Materials & Design 247 (2024) 113412

Contents lists available at ScienceDirect

Materials & Design

journal homepage: www.elsevier.com/locate/matdes

Fatigue and short crack assessment of powder bed fusion laser-based fabricated AlSi10Mg miniature specimens under alternating bending load

Sebastian Stammkötter [a,*], Jochen Tenkamp [a], Mirko Teschke [a], Kai Donnerbauer [a], Alexander Koch [a], Timo Platt [b], Dirk Biermann [b], Frank Walther [a]

[a] Chair of Materials Test Engineering (WPT), TU Dortmund University, Baroper Str. 303, D-44227 Dortmund, Germany
[b] Institute of Machining Technology (ISF), TU Dortmund University, Baroper Str. 303, D-44227 Dortmund, Germany

ARTICLE INFO

Keywords:
Al-Si alloy
Additive manufacturing
Fracture mechanical approach
Bending
Miniaturization

ABSTRACT

Al-Si alloys are commonly used in the automotive and aircraft industry because of their excellent strength-to-weight ratio. Due to the laser powder bed fusion manufacturing process, inhomogeneous cooling affects the microstructure as well as defect distributions. Within this paper, the uniform fatigue damage tolerance assessment was further qualified for (miniature) bending specimens with different loaded volumes based on the concepts according to Murakami ($\sqrt{area}$) and Shiozawa for an initial defect-based model. These approaches were used to calculate defect-related fatigue life curves, in which the cyclic stress intensity factor (ΔK) at the initiating defect ($\sqrt{area}$) was used to represent local stress concentration at the crack tip instead of nominal stress-based S-N curves. Results of S-N curves did not allow a precise lifetime prediction due to increasing effect of manufacturing-related defect distributions, while fracture mechanical approaches enable a uniform fatigue lifetime description of different testing volumes. The calculated fatigue limit and short crack threshold value suggested by Noguchi based on the extended approach of Murakami need to be compared and validated experimentally. Furthermore, the effects of miniaturization and crack propagation have been identified and considered. Uniform fatigue life predictions and efficient materials testing have been combined and show potential for future research.

1. Introduction

Due to cost and resource efficiency, the process of additive manufacturing (AM) enables the precise production of large and small-scale near-net-shape components with increased complexity [1]. Changes in parameter and scanning settings during the manufacturing process lead to the adjustability of the microstructure and can consequently affect the mechanical properties [2]. With the powder bed fusion laser-based process (PBF-LB) improved surface roughness and lower production costs can be achieved compared to the electron beam powder bed fusion (PBF-EB) process [3]. While conventionally manufactured parts are used in automotive or railway industries, AM components will be used for customized parts with high functionality and complexity in medical or space applications [4]. Additionally, they are not only used for prototyping but also transferred to functional parts which enables new possibilities [5].

Aluminum-silicon-alloys like AlSi10Mg are typically used in cast state but can also be used in AM processes due to their excellent strength-to-weight properties. The investigated alloy belongs to the hypoeutectic alloy because of its Si percentage (<12 wt%) with very good melting properties. Besides the microstructural properties, the mechanical loading depends on process-related defects like intermetallic phases, oxides, porosity, and the building direction of the AM process.

Due to the manufacturing, process-related defects such as gas pores or lack of fusion defects can be reduced mostly but not fully avoided. Therefore, these defects need to be considered and were investigated in some previous studies for AlSi-alloys where the high cycle and very high cycles fatigue regime was characterized for additively manufactured materials [6–8]. Further works [9,10] emphasized the effects of defects on uni-axial fatigue properties. They showed approaches for defect-based modeling and lifetime predictions using fracture mechanics for AlSi10Mg. Additionally, investigations were conducted by Roveda et al. [11] and Baig et al. [12] in the case of heat treatment effects on short crack behavior and fatigue properties of aluminum alloy which will be further developed in this work. For a resource-efficient experimental determination of the Woehler (S-N) curve, Nicoletto et al. [13,14] invented a miniature bending fatigue testing (MBFT) routine which led

* Corresponding author.
E-mail address: sebastian.stammkoetter@tu-dortmund.de (S. Stammkötter).

https://doi.org/10.1016/j.matdes.2024.113412
Received 11 September 2024; Received in revised form 16 October 2024; Accepted 24 October 2024
Available online 28 October 2024

Nomenclature

a_i	Failure-initiating defect size
a_p	Cutting depth
b	Height of specimen
C	Shiozawa coefficient
$C_{Al,N}$	Surface stress factor according to Nicoletto
$C_{Al,C}$	Self-determined surface stress factor
CAT	Constant amplitude test
d	Diameter
E	Young's modulus
E_{Al}	Young's modulus of aluminum
E_{St}	Young's modulus of steel
EBSD	Electron backscatter diffraction
F	Force
f	Test frequency
h	Width of specimen
HCF	High cycle fatigue
HV	Vickers hardness
ΔK	Cyclic stress intensity factor
ΔK_i	Cyclic stress intensity factor at failure-initiating defect
$\Delta K_{th,int}$	Intrinsic threshold for short cracks
$\Delta K_{th,C}$	The critical threshold of experimentally determined short cracks
$\Delta K_{th,C}^{Ref}$	Modeled critical threshold of short cracks (reference condition)
$\Delta K_{th,C}^{AM}$	Corrected model of critical threshold of short cracks for AM condition
M	Bending moment
m	Shiozawa exponent
n	Spindle speed
N	Number of cycles
N_f	Number of cycles to failure
R	Stress ratio
R^2	Coefficient of determination
r_ε	Corner radius
s_{min} / s_{max}	10 % and 90 % error bands
S	Sphericity
T	Scatter range
$\Delta\sigma$	Stress range
σ_a	Stress amplitude
σ_{max}	Maximum stress
σ_{aL^*}	Modeled fatigue limit according to Noguchi
VHCF	Very high cycle fatigue
v_c	Cutting speed
v_f	Feed velocity
W	Moment of resistance

to similar S-N curves compared to uni-axial fatigue testing. These works focused on variant surface roughnesses caused by different post-processing methods such as polishing, as-built surfaces, or machining. In addition to other surface conditions, Nicoletto et al. [15] also investigated the effects of various building and loading conditions and the direction and notch effects [14] on the small-scaled specimens. Such innovative miniature concepts with environmental aspects and material savings underline the importance of these efficient strategies. The testing routine will be evaluated and extended for the crack propagation behavior of additively manufactured AlSi10Mg within this study and will be compared to the literature.

In addition to the conventional determination of Woehler curves, for crack propagation dominated behavior, approaches according to Shiozawa and Murakami [16,17] can be used to include the defect size and normalize the lifetime. To describe the crack propagation behavior mathematically, the Paris-Erdogan law including the failure-initiating defect size a_i can be transformed according to Eq. (1) [16]:

$$\Delta K_i = \left[\frac{C(m-2)}{2}\right]^{-1/m} \cdot \left(\frac{N_f}{a_i}\right)^{-1/m} = K_f^{'} \cdot \left(\frac{N_f}{a_i}\right)^{d} \tag{1}$$

The coefficient C and the exponent m can be calculated by using power law fit while plotting cyclic stress intensity factor (SIF) (y-axis) over the number of cycles to failure N_f divided by the initial defect size a_i which can be defined as a defect-related number of cycles to failure (x-axis). The SIF can be calculated by Murakami's approach [17], see Eq. (2):

$$\Delta K_i = \Delta\sigma \cdot \sqrt{\pi \cdot a_i} \cdot Y \quad Surface: Y = 0.65;\ Volume: Y = 0.50 \tag{2}$$

Consequently, the fatigue behavior can be represented in a log–log plot as a line curve (K-N) analogously to classical S-N curves. According to alternate bending testing as an appropriate alternative for uni-axial testing of miniaturized specimens, the stress concentration needs to be considered. The integration or enhancement of the miniature bending fatigue testing (MBFT) routine by fracture mechanical models is new in general and will be evaluated for AlSi10Mg due to material and time-saving aspects. Therefore, when applying SIF-based approaches, the distance of the failure-initiating defect to the surface needs to be measured and included because of the graded stress concentration during alternate bending. The bending moment and resulting nominal stress were equally transformed according to the definition in Eq. (3) in which the nominal bending moment M and moment of resistance W need to be considered. B and h represent the height and the width of the miniature specimen testing area and σ_{max} represents the maximum stress on the specimen's surface.

$$\sigma_{max} = \frac{M}{W} \quad \text{with } W = \frac{(b \cdot h^2)}{6} \tag{3}$$

For crack propagation investigations, the application of artificially induced notches via micro milling at mini-bending specimens will be tested to characterize the short crack behavior of AlSi10Mg. The intrinsic threshold $\Delta K_{th,int}$ can be calculated by using Young's modulus E according to the literature [18], see Eq. (4):

$$\Delta K_{th,int} = 1.6 \cdot 10^{-5} \cdot E \tag{4}$$

In addition to experimental threshold determination of $\Delta K_{th,C}^{AM}$, a numerical approach according to Murakami [17] with an extension of Noguchi [19] will be used Eq. (5) and compared:

$$\Delta K_{th,C} = C \cdot \left(HV + 120 \cdot \frac{E_{Al}}{E_{St}}\right) \cdot \sqrt{area}^{\frac{1}{3}} \tag{5}$$
$$Surface: C = 0.00027;\ Volume: C = 0.00030$$

Investigations of Murakami [20] and Ueno [21] validated that fatigue limit increases the defect size for aluminum alloys.

$$\sigma_{aL^*} = \frac{C \cdot \left(HV + 120 \cdot \frac{E_{Al}}{E_{St}}\right)}{a_i^{\frac{1}{6}}} \tag{6}$$
$$Surface:\ C = 1.43;\ Volume:\ C = 1.56$$

In this approach, different parameters like the hardness HV, the Young's modulus of aluminum E_{Al} and steel E_{St} will be taken into account. The effects of miniaturization and especially the short crack propagation behavior should be investigated with a focus on resource efficiency and improved testing methods for appropriate and reliable

Table 1
PBF-LB/M scanning parameters for AlSi10Mg using TruPrint 1000 machine.

Laser power [W]	Scanning speed [mm/s]	Hatch distance [µm]	Layer thickness [µm]	Beam diameter [µm]	Scanning rot. angle [°]	Pre-heating temperature [°C]
175	1,550	90	20	55	90	180

Table 2
Chemical composition (wt.%) of additively manufactured AlSi10Mg.

Al	Si	Fe	Cu	Mg	Ni	Zn
Bal.	10.93	0.19	0.02	0.38	0.01	0.02

testing of safety components.

To perform quantitative evaluations on the fatigue results, the scatter range T was introduced and can be calculated out of 10 % (s_{max}) and 90 % (s_{min}) survival probability by using the following equation:

$$T = \frac{s_{max}}{s_{min}} \tag{7}$$

2. Experimental methodology

2.1. Materials and manufacturing process

The AlSi10Mg samples were additively manufactured by Laser Powder Bed Fusion (PBF-LB/M) using the Trumpf TruPrint 1000 (Trumpf, Germany) AM machine. The manufacturing was performed at Fraunhofer IAPT (Germany). The parameters for the manufacturing process are summarized in Table 1.

The chemical composition of AlSi10Mg was determined and statistically validated using the OES 720 system (Hitachi, Japan) and is given in Table 2.

All specimens were characterized in as-built conditions without heat treatment. The specimens were manufactured into the final geometry by turning and wire-cut EDM (Fig. 1a/c). Afterward, samples were ground and polished to reduce the influence of roughness-induced failure during fatigue testing. Due to sustainability and material-saving aspects, the geometry of mini specimens (AM-10-M) (Fig. 1b) which was inspired by Nicoletto [13,15] was machined from the rear parts of tested standard bending specimens (AM-10-S) which highlights the aspect of material saving and efficiency.

2.2. Pre-test preparation and machine clamping

Resource efficiency and thus material and cost savings often go hand in hand with other challenges. Before mechanical tests can be conducted, different preparation steps need to be performed. Challenges in grinding and polishing have to be managed to prevent possible influences of surface roughness. Therefore, all sides of the mini specimens were polished after the machining process.

2.3. Notch initiation via micro milling for crack propagation tests

For appropriate crack propagation testing of miniaturized specimens, a micronotch is necessary according to ASTM E647 to weaken the specimens' surface. V-shaped notches at the specimen corner with a notch angle $\phi = 60°$ were therefore selected to see crack propagation on top and side of the specimen. The preparation was carried out using a CNC precision machine tool (KERN Microtechnik, type HSPC 2522) with sufficient capabilities in terms of spindle speed (up to $n = 50{,}000$ rpm), working accuracy (± 2.5 µm) and positioning accuracy (± 1.0 µm). To obtain a crack propagation of the notched samples, a circular ground of the notch was aimed. Cutting tools developed for thread machining (cutting angle 60°, corner radius $r_\varepsilon = 50$ µm) were used for this purpose (Fig. 2a). A feed direction symmetrical towards the corner of the sample was selected as a cutting strategy. Final notched specimens with cutting depths ap of 200 µm were investigated and are shown in Fig. 2b. To characterize the prepared sections and the depth for reliable and complex defect size calculation, the sample surfaces were digitized using a confocal microscope (Confovis, type ToolInspect). The geometry of the V-shaped corner notch and its tip as well as the circular ground were realized according to the cutting tool used. Fig. 2c and Fig. 2d show the CAD calculation of the notch size and the real geometry. Using this method, notches could be precisely machined with a high accuracy in terms of cutting depth.

2.4. Mechanical testing and crack propagation test

During this study, two different specimen geometries were investigated using a resonant fatigue testing system Rumul Cracktronic with a

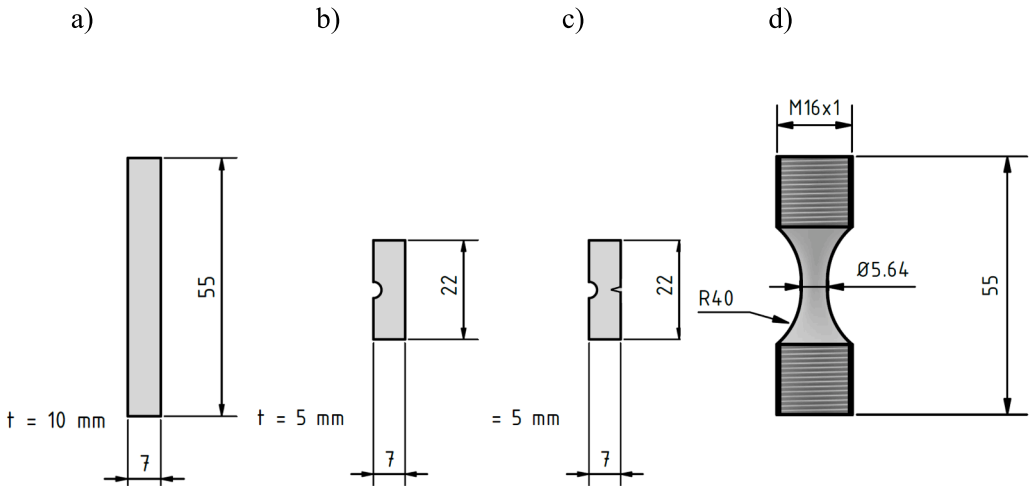

Fig. 1. (a) Standard bending specimens (AM-10-S), (b) miniature specimens (AM-10-M) for testing (adapter necessary),(c) micro-notched miniature specimens (only for crack propagation test), and (d) specimen geometry for uni-axial testing.

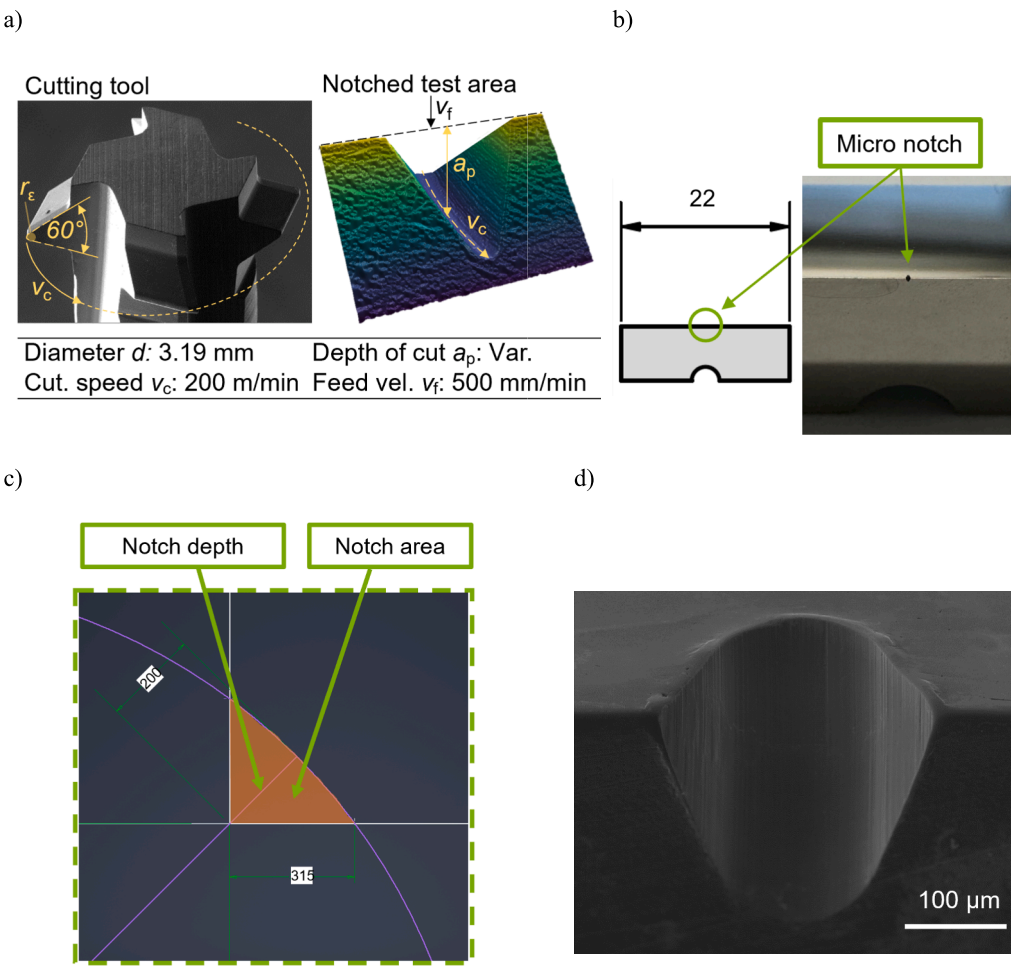

Fig. 2. Defect initiation through micro-milling: a) Geometry of milling tool followed by surface determination with a confocal microscope, b) notched mini-bending specimen before testing, c) CAD geometry, and d) real notch after process using SEM.

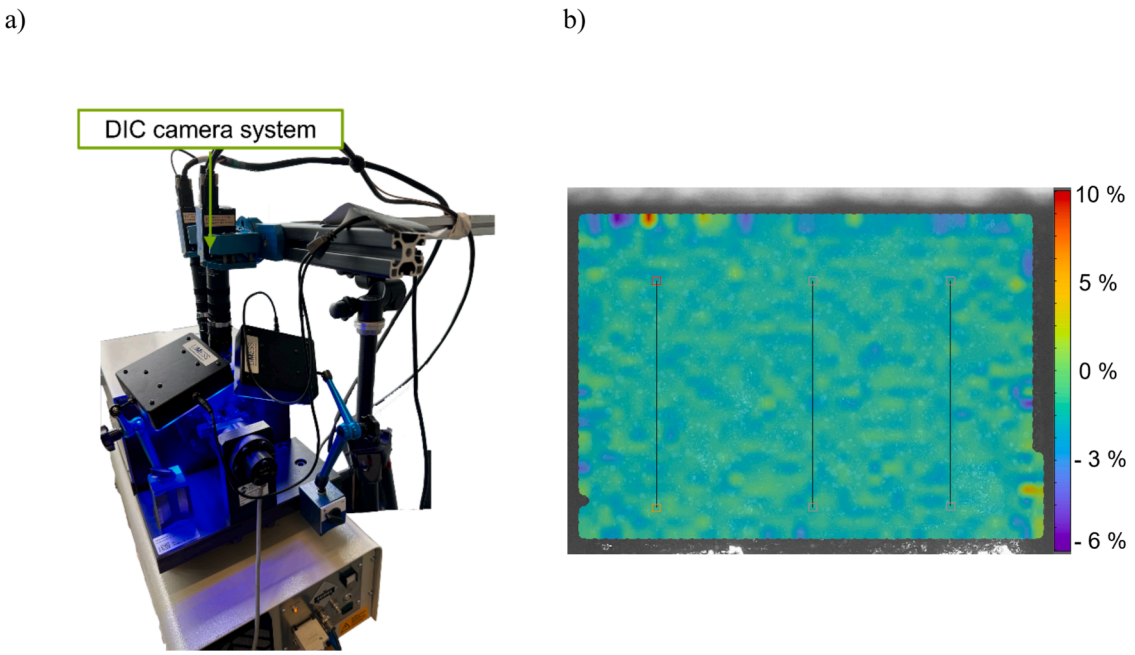

Fig. 3. a) DIC camera system for true stress measurements on surface and b) strain calculation method on specimens surface for stress determination.

Table 3
Parameters of μ-CT investigations for AlSi10Mg.

Beam current [μA]	Beam energy [kV]	Power [W]	Working distance [mm]	Effective pixel size [μm]	Voxel size [μm]	Exposure time [ms]	Exposure rate [fps]
100	135	13.5	124	11.5	11.0	354	2.82

70 Nm load cell at a frequency of 80 ± 5 Hz. The fatigue behavior was characterized in moment-controlled constant amplitude tests (CAT) at a load ratio of $R = 0.1$. The maximum bending stress at the surface is set in a defined manner by measuring the exact height and width and adjusting the bending moment accordingly. Uni-axial fatigue tests were performed on a resonant fatigue testing system Rumul Testronic with a 20 kN load cell at a similar frequency and load ratio. For surface stress determination, DIC system Q400 (Limess, Germany), 50 mm objectives with a resolution of 5 MP was fully used (Fig. 3) to detect elastic strains on the specimen's surface to evaluate the applied stress compared to the nominal bending moment. The stress calculation was performed using Hooke's law for the linear-elastic regime. The facet size was chosen at 39 with a grid spacing of 20.

For further characterization of (short) crack propagation behavior, cyclic resistance curve tests were performed on mini-bending specimens. Tests were conducted for resource-efficient short crack characterization in case of specimen size. The initial defect size was determined to be $a_i = 131\mu m$ (calculated out of the cutting depth a_p) and a value of 75 % of the intrinsic threshold was chosen as the initial stress intensity factor. The a_i was reached by using a notch cutting depth of 200 μm and then calculating the cross section using CAD software due to the high precision of the notch manufacturing process. The intrinsic threshold $\Delta K_{th,int}$ was calculated using Eq. (4) and it could be found that no crack propagation occurs below $\Delta K_{th,int}$. Resonant frequency as well as digital microscope Keyence VHX 7000 was used for validating no crack growth below $\Delta K_{th,int}$. The single specimen test was performed with increasing ΔK, provided that no crack propagation occurred.

2.5. Computed tomography, fractographic analyses, and electron backscatter diffraction

Before the mechanical investigations, a computed tomography scanner Nikon XT H160 (Japan) was used for 3D-pore-analysis with software VG StudioMax 2024.2.1 to determine defect density and distribution in the mini-bending specimens. CT scanning parameters are listed below in Table 3.

For the determination of the crack-initiating defect as a prerequisite for applying fracture mechanical approaches, post-mortem analyses in an SEM Tescan MIRA3 XMU are necessary. The fractured surfaces were investigated to identify critical defects and derive failure mechanisms. Failure-initiating defects were characterized using ImageJ software. In addition to that, EBSD and EDS scans were conducted during the SEM investigations using an EDAX Velocity Plus detector to show the microstructural effects of the additive manufacturing process on the crack propagation behavior.

3. Results and discussion

3.1. Microstructure and defect distribution of mini-bending specimens

The microstructure of as-built AlSi10Mg consists of a cellular structure because of fast cooling during the additive manufacturing process [22]. The average α-Al cell diameter is estimated to be 0.5 μm and was determined by SEM investigations. In the as-built state of AlSi10Mg, α-Al cells are divided by eutectic silicon phases with a diameter approximately between 55 and 90 nm as shown in Fig. 4. The arrangement and structure of the eutectic silicon phase are specific for the as-built condition of AlSi10Mg and exhibit a spatially inhomogeneous shape [23]. Partially large accumulations of Si in the node region are contrary to significantly small amounts in the strut regions. Additionally, no effects of Si accumulations on micro-cracks can be identified. To gain information about the element compositions and distribution in the characteristic phases, energy dispersive x-ray spectroscopy (EDS) was conducted. Spectrum analyses of specific spots in Si-rich eutectic phases as well as the α-Al network indicate differences in element distributions but do not show any correlation in case of crack propagation.

In addition to that, microstructural characteristics like hardness (HV10) and failure-initiating defect sizes were investigated and compared between different specimen geometries. Macro hardness patterns show no significant differences due to the same manufacturing process and building direction. The failure-initiating defect size, and the

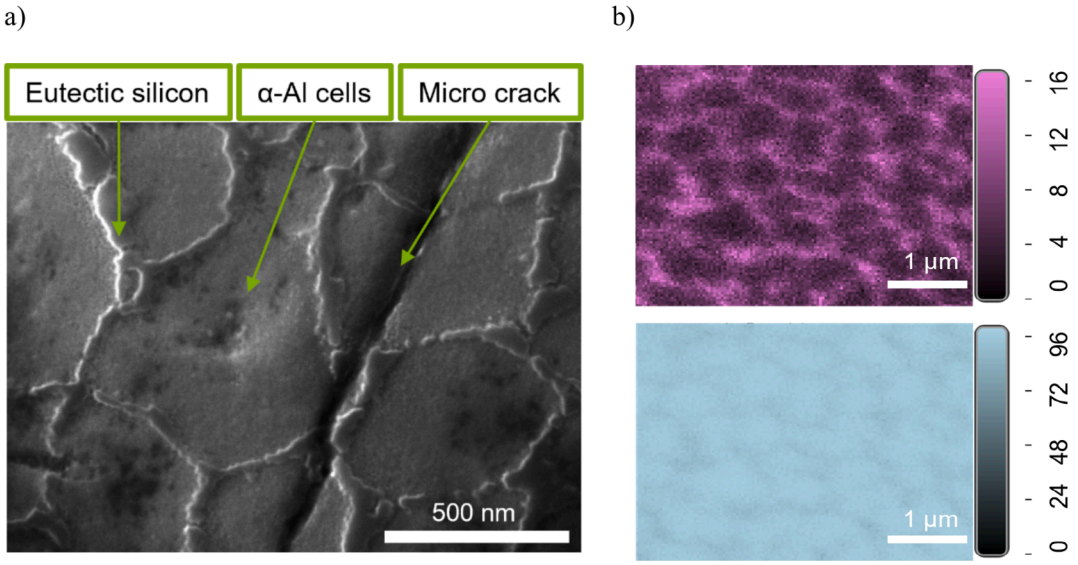

Fig. 4. a) SE-SEM micrograph of mini-bending specimen AlSi10Mg with eutectic silicon phase, α-Al cells, and microcrack at a magnification of 140-k and 25 kV beam energy and b) EDS phase mapping for Si- and α-Al network.

Table 4
Microstructural characteristics of AlSi10Mg bending specimens.

Batch	HV10 [kgf/mm^2]	Failure-initiating defects [µm]	Specimen volume [mm^3]
AM-10-S	136 ± 1	191 ± 24	3850
AM-10-M	134 ± 3	161 ± 13	770
AM-10-A	130 ± 5	221 ± 31	7700

specimen volume listed in Table 4 are not comparable between the different geometries. The post-mortem analyses of mini-specimens show a reduced failure-initiating defect size of approx. 20 % compared to standard bending specimens due to smaller specimen volume and reduced defect distribution.

µ-CT scans were carried out and analyzed for non-destructive characterization of defect distributions. The evaluations show that the defect distributions are slightly inhomogeneous regarding the surface distance. Fig. 5 shows the defect distributions and locations of different specimen types. Failure-initiating defect positions can affect the fatigue limit or lifetime and become more relevant when applying bending loads compared to standard multi-axial testing as this cross-section has a homogeneous stress distribution.

As already illustrated in µ-CT analyses, differences in defect distributions could be attributed to the reduced sample volume of mini specimens and consequently to a lower probability for lack of fusion defects. This can be proven by evaluating the sphericity and the absolute frequency of the defects. Fig. 6 emphasizes the defect sizes concerning the sphericity and the absolute frequency of the three different testing geometries. Predominant equivalent defect sizes are very small and show a high sphericity which suggests that they can traced back to gas porosity [24]. The equivalent defect size was determined using the diameter given by CT evaluation and sphericity. Furthermore, the effective 2D area of the defect was calculated and then the square root was applied to archive the equivalent defect size a_i. The number of lack of fusion defects, which can be mostly identified by their size and sphericity (mostly between 0–0.4) [24], are comparatively low. Investigations of Wu et al. [25] showed the effects of processing parameters on defect shape and location during manufacturing. Romano et al. [26] also focused on µ-CT pre-tests to gain 3D information about the defect distribution which can be compared with fractography results after fatigue tests. The dependence of sphericity and equivalent defect size indicates the type of defect that is related to the manufacturing strategy and building direction shown in the results of Larrosa et al. [27]. Fig. 6 shows the equivalent defect size distribution and the appearance of critical defects, which was also performed in other studies [9,27,28]. The dashed line shows the average initial failure defect size a_i of the tested specimens which were determined out of the fracture surface via ImageJ software and compared to µ-CT data. When comparing the different defect distributions of the geometries, the effect of the specimen volume can be identified and supported by the extreme value distribution of the LogNormal function. For AM-10-M there is a decreased number of defects which are bigger than $a_i > 300$ µm compared to AM-10-S or AM-10-A. In addition to the sphericity, the total number of defects also supports the argument of a reduced number of lack of fusion defects when investigating smaller testing volumes.

3.2. *Effects of miniaturization on fatigue behavior and cyclic stress intensity factor (SIF)*

To evaluate the fatigue performance of different specimen geometries in terms of the miniaturization strategy for sustainable testing, constant amplitude tests (CAT) were conducted. The investigations showed major differences regarding the S-N curves of the mini and standard bending specimens. Investigations by Nicoletto [15] showed that mini specimens reveal an overestimation of surface stress of factor $C_{Al,N} = 0.9$ compared to the nominal applied stress set in the machine. To rule out a machine-specific stress coefficient, validation measurements of the stress concentration at the specimens' surface were performed using the 3D-DIC measurement method. The tests were carried out in the elastic range to safely reach non-plastic strains and convert them, via Young's modulus, into stresses to evaluate the real stress concentration on the surface. The determined stress difference factor on Rumul Cracktronic was determined for AlSi10Mg to be $C_{Al,C} = 0.88$ while using the specific miniature adapter. Compared to Nicoletto's results, the correction factor determined for this study shows no significant difference.

For comparing the fatigue behavior, different S-N curves of AlSi10Mg are presented in Fig. 7a and show the effect of miniaturization. Batch AM-10-M-In represents the initial testing results before DIC factor determination, therefore the corrected S-N curve (−12 %) with a correction factor of $\sigma_{a,eff} = \sigma_a \cdot 0.88$ (batch AM-10-M) (Fig. 7a) can be subsequently used for further figures. The S-N curve of batch AM-10-S represents standard bending specimens (Fig. 1a), which were tested under constant stress amplitude at a stress ratio of $R = 0.1$. Both conditions (AM-10-M and AM-10-S) show a comparable fatigue behavior in the lower HCF regime, but increasing deviations in the higher HCF regime. There was one outlier in the test after run-out, which showed a proven deviation in the defect structure compared to all other miniature samples. The slope of the tested batches is different, therefore a uniform HCF assessment of standard and mini-bending specimens is not possible.

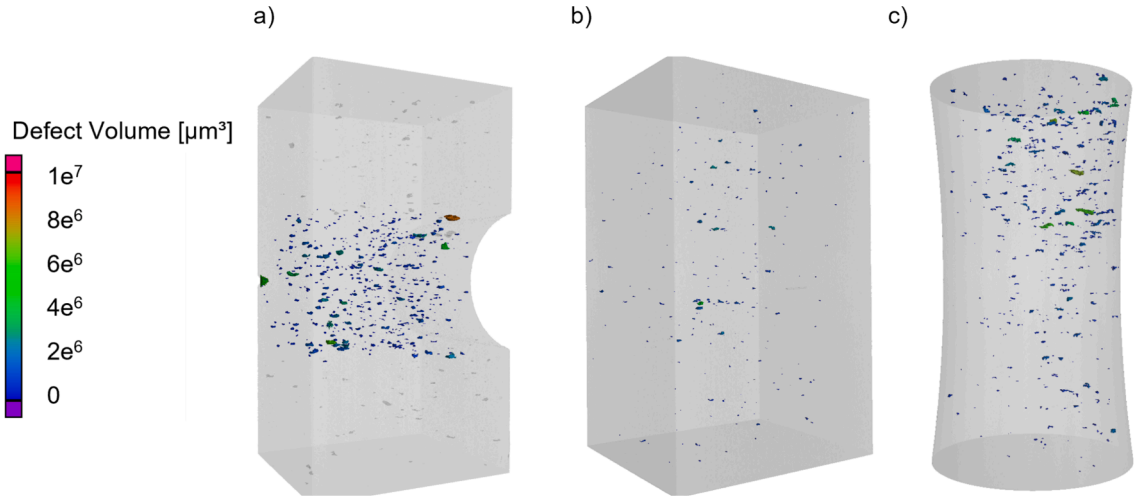

Fig. 5. µ-CT scan for AlSi10Mg a) mini-bending, b) standard bending, and c) uni-axial specimen for 3D-pore-analysis.

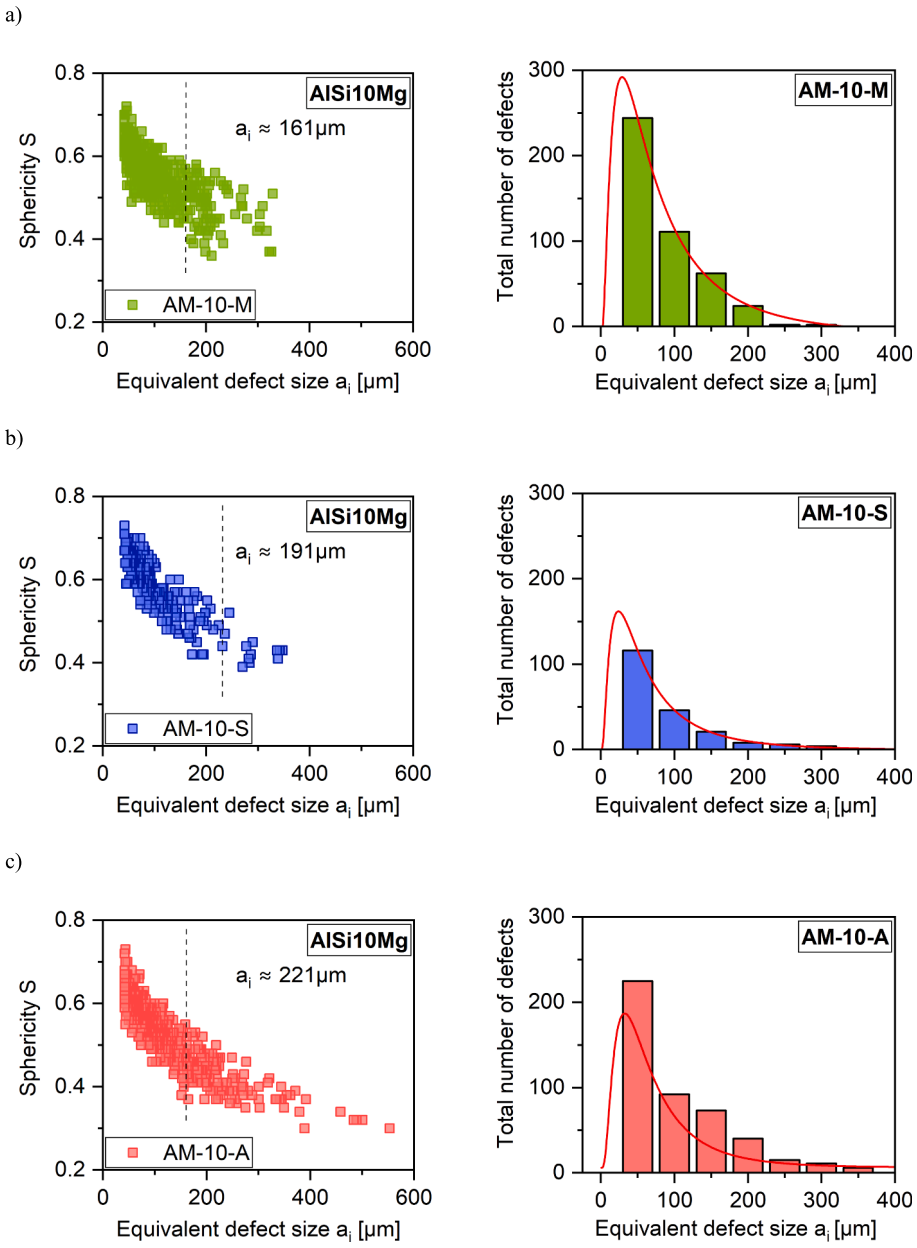

Fig. 6. Evaluations of µ-CT scans of a) mini-bending b) standard bending and c) uni-axial testing of AM-AlSi10Mg specimens with LogNormal extreme value distributions.

For statistical evaluation of the Basquin fits for S-N curves, coefficient of determination (R^2) and 90 % scatter bands were introduced and showed high precision and confidence. Comparing the averaged initial defect sizes a_i of both conditions which were calculated out of the fracture surface in ImageJ software, it can be concluded that mini-bending specimens show reduced defect sizes of about 19 %. As a result of smaller specimen volumes, the probability for larger defects will potentially decrease (shown in µ-CT investigation of Fig. 6) and can explain the increased fatigue performance in Fig. 7 for a higher number of cycles and the smaller average defect size a_i of mini-bending specimens ($N \approx 10^6$). Additionally, the failure-initiating defect sizes for all specimens are listed in Table 5 to show the effect of defect size on fatigue behavior. Due to the mentioned differences in S-N curves between the types of specimens, the uniform interpretation of standard and mini-bending specimens has to be further investigated using defect-tolerant concepts which require critical defect area measurements (Fig. 7b).

To evaluate the failure-initiating defect sizes of different specimen geometries, Table 5 shows critical defect sizes during CAT. The critical defects were observed via SEM and assessed using ImageJ software for shape and area calculations.

Preliminary investigations [29–31] already showed a positive effect of using fracture mechanics approaches such as curves according to Shiozawa based on the concept of Murakami for uniform fatigue tolerance of uni–axial testing of Al-Si alloys. To extend and validate the use of these defect-based assessments, the transferability to (mini-)bending specimens is investigated. Fig. 8 shows the so-called Shiozawa curve (K-N curve) in which the cyclic stress intensity factor (SIF) is plotted over the quotient of the number of cycles to failure N_f and initiating defect size N_f / a_i (x-axis). The K-N curve for the batch of mini-bending specimens shows an appropriate slope with a typical value for Paris exponent m for Al-alloys of 5.2 while the exponent for uniform prediction is slightly reduced. Using the defect-based approach of Murakami, the fatigue damage tolerance assessment of mini and standard bending conditions is significantly improved and can be validated for AlSi10Mg

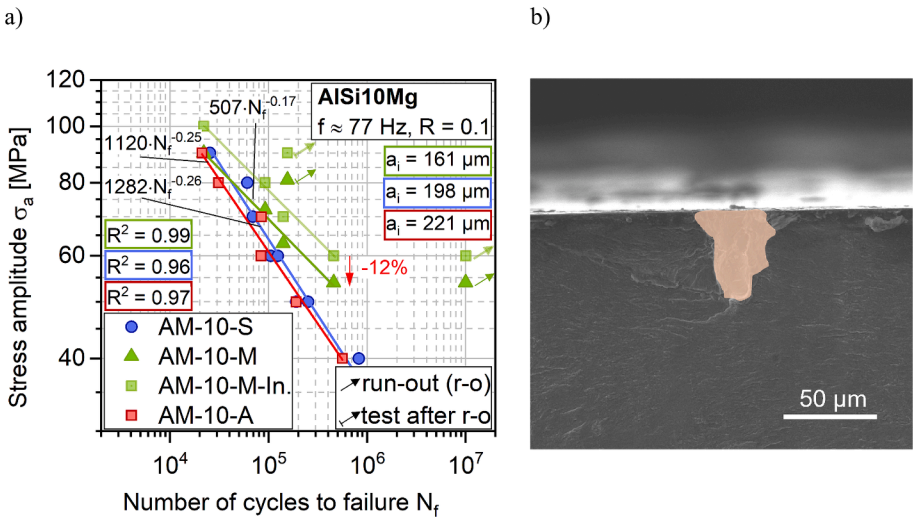

Fig. 7. a) Comparison of Woehler (S-N) curves for i) standard bending (AM-10-S), ii) initial mini-bending (AM-10-M-In), iii) corrected mini-bending (AM-10-M) and iv) uni-axial testing specimens of AlSi10Mg with b) SEM fractography of failure-initiating defect.

Table 5
Failure-initiating defect sizes of different testing geometries AM-10-M, AM-10-S, AM-10-A.

Stress amplitude σ_a [MPa]	Failure in. defect size a_i [µm]	Stress amplitude σ_a [MPa]	Failure in. defect size a_i [µm]	Stress amplitude σ_a [MPa]	Failure in. defect size a_i [µm]
100	210	90	247	90	228
80	183	80	140	80	198
70	178	70	230	70	239
60	138	60	193	60	281
60	100	60	198	50	213
		50	207	40	171
		50	185		
		40	193		

bending specimens. Furthermore, the intrinsic threshold can be determined with $\Delta K_{th} = 1.7$ MPa$\sqrt{m}$ for mini specimens and $\Delta K_{th} = 1.3$ MPa$\sqrt{m}$. Due to variances in critical defect sizes of mini- and standard bending specimens, the determined threshold is different for these geometry types. AM-10-S specimen shows a larger critical defect size, therefore a smaller stress amplitude is necessary for failure, consequently the SIF will be lower than for the mini-specimen. These results indicate that differences in S-N curves are caused by different defect distributions of mini-bending specimens and can be included in fracture mechanics.

Further benchmarking, classification, and integration of uni-axial and bending test results are shown in Fig. 9a. The Paris coefficient C

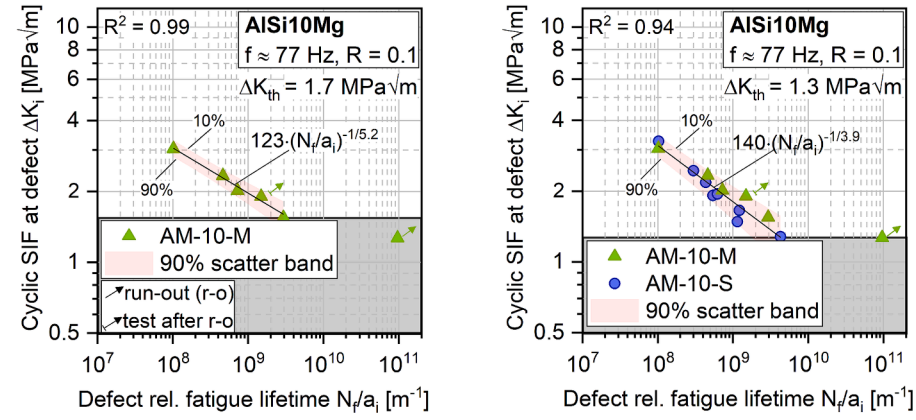

Fig. 8. a) Shiozawa (K-N) curves according to the approach of Murakami for mini-bending specimen, b) comparison cyclic SIF of mini and standard bending specimens of AlSi10Mg.

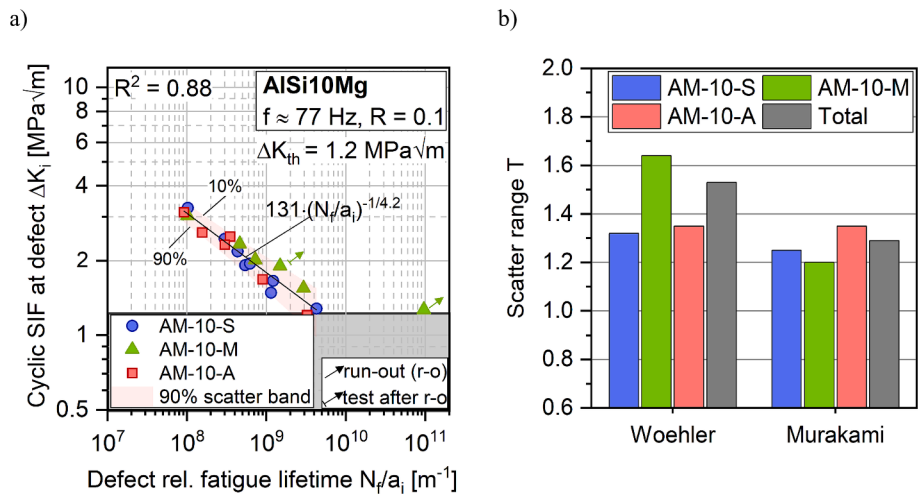

Fig. 9. a) Uniform Shiozawa (K-N) curve for all specimen types, b) quantitative evaluation of Woehler and Murakami approaches for different geometries of AlSi10Mg.

and exponent m can be determined using the power law fit of Eq. (1). The uniform Shiozawa curve shows an improved prediction of the fatigue life with high accuracy and no significant outliers. The intrinsic threshold against failure and damage initiation can be determined for a uniform assessment with $\Delta K_{th} = 1.2\ \mathrm{MPa}\sqrt{\mathrm{m}}$ which is comparable to the literature. [29].

When focusing on quantitative evaluations in Fig. 9b, the variation in the scatter range T between the integral approach of Woehler and the local concept of Murakami can be evaluated. For all specimen types, better accuracy and prediction can be identified by using a linear elastic fracture mechanics approach. According to previous studies, the positive effects of fracture mechanics approaches have been investigated [32,33]. Especially the decreasing T value, resulting from the scatter bands, for AM-10-M emphasizes the importance of fracture mechanics due to the significant effect of defect distribution combined with reduced specimen size on fatigue behavior. For uniform lifetime prediction of different testing volumes respectively specimen types, the approach of Murakami improves the prediction of damage tolerance and leads to good fatigue and threshold determination.

3.3. *(Short) crack propagation behavior of miniaturized AlSi10Mg specimens*

Previous studies showed that especially short cracks have a significant impact on fatigue properties [34]. In addition, micro-cracks grow at lower stress intensity threshold values than long cracks and consequently have to be strongly investigated and understood [35,36]. While conventionally produced specimens contain a high amount of slip bands in the crack tip area (Fig. 10b) [37], additively manufactured components show no slip band formation for as-built condition (Fig. 10a) because of Si-rich phase networks, grain boundaries, and critical defects which affect the dislocation behavior during crack propagation and the crack propagation process itself [23].

Based on the fractographic investigations of mini-bending and uni-axial specimen geometries, differences can be macroscopically detected. Fig. 11a shows a homogeneous crack initiation and propagation on the crack surface for constant cross-section specimens. In contrast, the surfaces of mini-bending specimens show a different and inhomogeneous crack propagation behavior due to a gradient stress distribution of bending load (Fig. 11b). The investigations indicate that crack initiation occurs at the largest and surface nearest manufacturing defects. Due to the neutral axis in the cross-section, the fatigue fracture surface is not comparable to those with uni-axial loading. Micro cracks mainly propagate in the surface plane, where the higher stresses apply. Crack growth inside the material is significantly less compared to growth on the surface and only occurs up to the neutral axis since testing was carried out at $R = 0.1$. Fig. 11b supports this assumption based on the geometry of the fatigue fracture surface. The crack length was determined using a high-resolution camera system for in-situ measurements. In addition to SEM fractography, EBSD scans were conducted to investigate microstructural effects on the crack propagation behavior of additively manufactured mini-bending specimens. As illustrated in Fig. 11c, AlSi10Mg

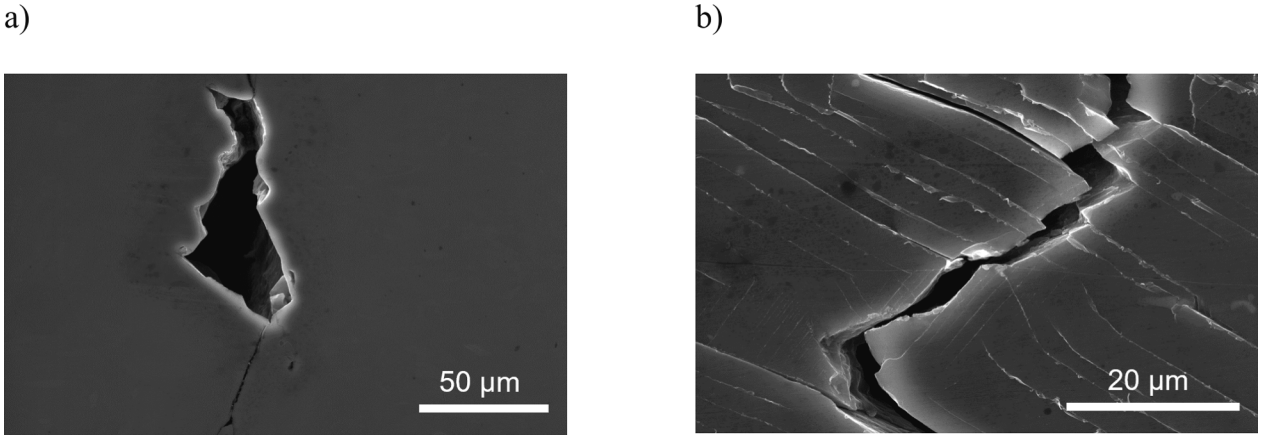

Fig. 10. Microcrack propagation of a) additively manufactured AlSi10Mg and b) conventionally produced cast alloy after fatigue test.

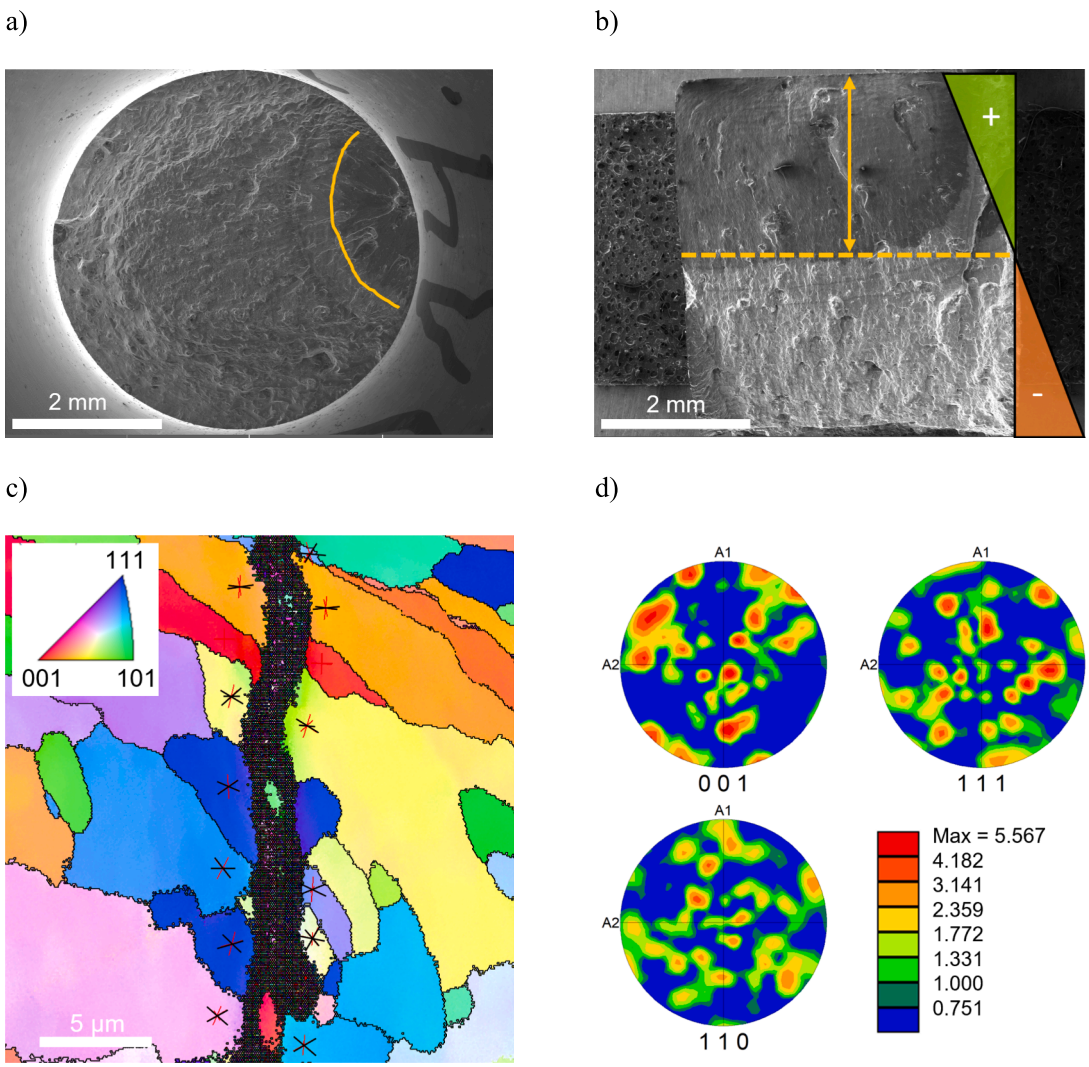

Fig. 11. SEM-fractography of a) standard uni-axial specimen, b) mini-bending specimen, c) inverse pole figures of mini-bending AlSi10Mg in crack area, determined by EBSD, and d) pole figures for the ODF.

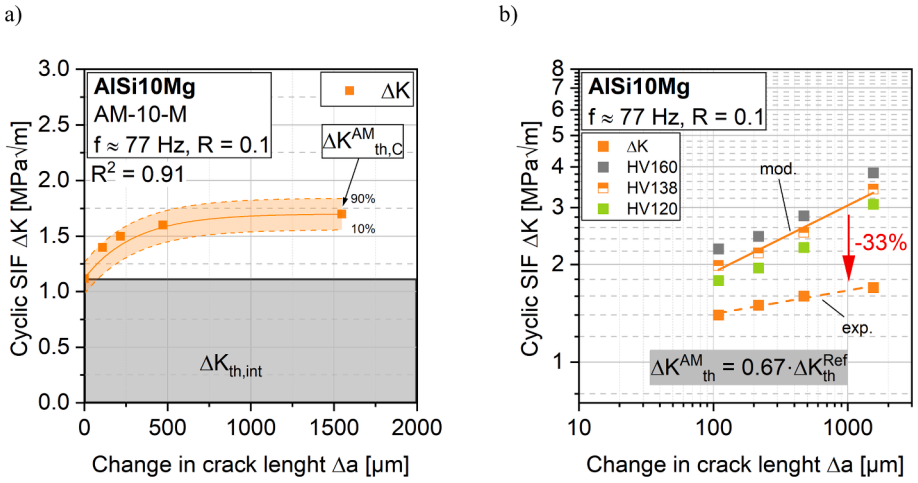

Fig. 12. a) Cyclic crack resistance curve and b) comparison of theoretical Murakami-Noguchi approach for long crack threshold with experimentally determined thresholds of AlSi10Mg.

shows transcrystalline crack propagation and is not affected by the build direction. The grain size is larger than the cellular structure. The microstructure shows an AM-specific fine-grain texture with different grain orientations. Black lines inside each grain show traces of {111}-sliding planes where red lines emphasize activated sliding planes. Due to lower necessary energy for {111} slip planes of fcc lattices, crack propagation will occur with shear stress controlled in the ⟨110⟩ direction. The investigated pole figures based on EBSD data from the crack region show no significant texture and therefore no correlation with crack propagation behavior (Fig. 11d).

To evaluate the short crack propagation behavior of mini-bending specimens, the aim was to adopt a micro notch. Fig. 12a shows the cyclic SIF ΔK versus the change in crack length Δa. The fitting curve was estimated using a modified NASGRO equation according to Maierhofer et al. [38] which was already applied by Pourheidar et al. [11,39] and shows good prediction ($R^2 = 0.91$). In addition, the scatter range T resulting from the ratio between 90 % and 10 % error bands is significantly small. The crack threshold was experimentally estimated to be $\Delta K_{th,C} = 1.71 MPa\sqrt{m}$ for AlSi10Mg. To compare experimental results with numerical estimations according to Murakami and the extension suggested by Noguchi which can be used for predictions of the fatigue limit as well as the threshold value [17,19], Fig. 12b shows a model-estimated approach based on hardness and defects. The curves are plotted as log–log functions. When comparing both, significant differences in model-based and experimental curves have to be considered. When calulating the value of $\Delta K_{th,C}^{Ref}$ the stress ratio has to be taken into account, since the approach is valid for $R = -1$. The difference between both curves leads to an approximated correction factor of $\Delta K_{th,C}^{AM} = 0.67 \cdot \Delta K_{th,C}^{Ref}$ which fits best in average to safely describe additively manufactured material behavior with the use of fracture mechanics model-based estimation. The results also show a reduced damage tolerance of about 33 % of additively manufactured Al-Si alloys which could be already investigated in the results of Tenkamp et al. [30].

3.4. Experimental validation and model transfer to previous studies l

For an appropriate design and prediction of safety-related components, a uniform fatigue damage tolerance model is necessary. In terms of experimental validation and proofing, the correction factor of 0.67 was applied to previous results of die-cast and additively manufactured specimens. Previous studies by Tenkamp et al. [30] showed uniform lifetime prediction of cast AlSi10Mg and AlSi7Mg. For validation, die-cast AlSi7Mg with different conditions is chosen and illustrated in Fig. 13a. It shows the relative S-N curves with the estimated fatigue limit Eq. (6) related to Murakami-Noguchi which can be also used for threshold determination Eq. (5). Consequently, the calculated correction factor can be equivalent transferred from the threshold determination of Fig. 12b to the fatigue limit and applied to Fig. 13. When comparing both curves, a reduced fatigue limit of additively manufactured components (PBF) to conventionally die-cast produced parts (DC1-3) could have been investigated. Using the improved model-based assumption in Fig. 13b, both conditions can be uniformly estimated and predicted using the same approximated and corrected fracture mechanical/fatigue limit approach (1/0.67) independent of material composition and manufacturing process.

4. Conclusions and outlook

The effect of process-induced defects of scaled additively manufactured mini-bending specimens was investigated and analyzed to develop a resource-efficient testing strategy using small specimens. The aluminum alloy AlSi10Mg was characterized in as-built condition under alternate bending load to analyze the effects of miniaturization on the fatigue properties, which is necessary to trace the results back to uniaxial loading of conventional specimens.

The fatigue behavior was characterized by a specific stress ratio using S-N curves and compared to the standard. Due to differences in fatigue behavior of miniaturized and standard specimens, a uniform prediction in the HCF regime was not reached.

The fracture mechanics approach according to Murakami was used and failure-initiating defects were considered to calculate the cyclic stress intensity factor (SIF) at the defect to improve the lifetime assessment.

The experimentally determined SIF threshold limit was compared to the model-based approach of Murakami-Noguchi and clearly showed a reduced limit of approximately 33 % for additively manufactured AlSi10Mg compared to conventionally produced parts. It could be shown that the short crack propagation rate of AlSi10Mg is significantly reduced as well as the fatigue limit due to different testing volumes and defect distributions.

Finally, the approximated difference factor of 0.67 (33 %) was used and applied for validation of previous studies in the case of uniform lifetime predictions for AM and cast conditions.

Therefore, the determined and to the specific load ratio converted factor leads to a uniform description of the fatigue and threshold limit for different manufacturing processes and enables a further improvement of standardized damage tolerance assessments.

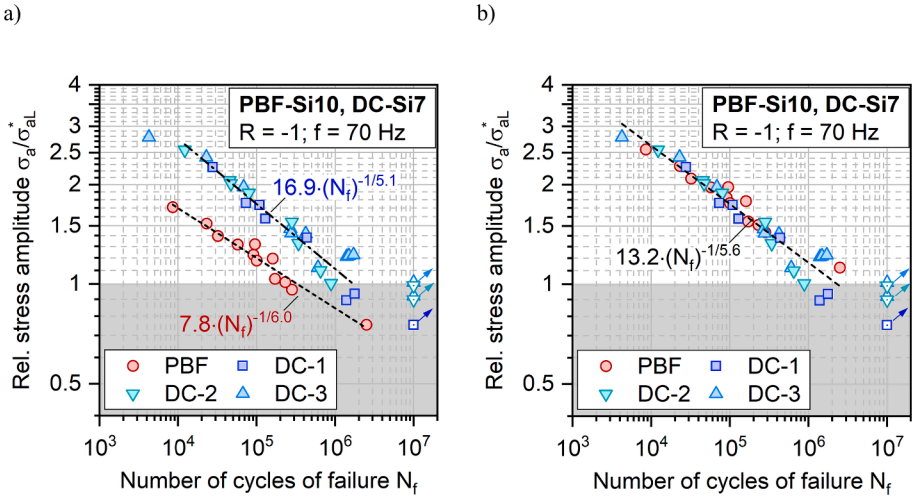

Fig. 13. Validation of experimentally determined correction factor: a) Relative S-N curves for AM (PBF) and die-cast (DC) [25] and b) uniform assessment of different manufacturing techniques.

CRediT authorship contribution statement

Sebastian Stammkötter: Writing – original draft, Visualization, Investigation, Formal analysis. **Jochen Tenkamp:** Writing – review & editing, Resources, Methodology, Conceptualization. **Mirko Teschke:** Writing – review & editing, Data curation. **Kai Donnerbauer:** Writing – review & editing, Software, Investigation, Data curation. **Alexander Koch:** Writing – review & editing, Visualization, Conceptualization. **Timo Platt:** Writing – original draft, Software, Methodology, Investigation, Data curation. **Dirk Biermann:** Writing – review & editing, Project administration, Funding acquisition, Conceptualization. **Frank Walther:** Writing – review & editing, Supervision, Resources, Project administration, Methodology, Funding acquisition, Conceptualization.

Declaration of competing interest

The authors declare that they have no known competing financial interests or personal relationships that could have appeared to influence the work reported in this paper.

Acknowledgement

Funding: The authors thank the German Research Foundation (DFG), Germany for its financial support within the research project “Data- and model-driven quantification of the interaction of defect distribution, atmosphere, and stress parameters during the HCF/VHCF damage evolution of age-hardenable Al-Si cast alloys” (project no. 496240495), the research unit FOR 5250 “Mechanism-based characterization and modeling of permanent and bioresorbable implants with tailored functionality based on innovative in vivo, in vitro and in silico methods”(project no. 449916462) and for their financial support within the Major Research Instrumentation Program for the CT-system Procon Alpha-Duo (project no. 459685720) and the in situ atomic force microscope (project no. 445052562). Further thanks to the Fraunhofer Research Institution for Additive Manufacturing Technologies (IAPT), Germany for the supply of specimen manufacturing within excellent scientific cooperation and Russenberger Prüfmaschinen AG (RUMUL), especially to Mr. Berchtold and Mr. Braun for outstanding support during this work.

Data availability

All raw/processed data required to reproduce these findings are available from the authors upon reasonable requests.

References

[1] X. Wang, S. Xu, S. Zhou, W. Xu, M. Leary, P. Choong, M. Qian, M. Brandt, Y.M. Xie, Topological design and additive manufacturing of porous metals for bone scaffolds and orthopaedic implants: a review, Biomaterials 83 (2016) 127–141.
[2] J. Gockel, L. Sheridan, B. Koerper, B. Whip, The influence of additive manufacturing processing parameters on surface roughness and fatigue life, Int. J. Fatigue 124 (2019) 380–388.
[3] S. Merkt, C. Hinke, J. Bültmann, M. Brandt, Y.M. Xie, Mechanical response of TiAl6V4 lattice structures manufactured by selective laser melting in quasistatic and dynamic compression tests, J. Laser Appl. 27 (2015).
[4] M. Javaid, A. Haleem, Additive manufacturing applications in medical cases: a literature based review, Alex. J. Med. 54 (2018) 411–422.
[5] A. Al Rashid, S.A. Khan, S.G. Al-Ghamdi, M. Koç, Additive manufacturing: technology, applications, markets, and opportunities for the built environment, Automation in Construction 118 (2020) 103268.
[6] Z. Jiang, J. Sun, F. Berto, X. Wang, G. Qian, Fatigue and fracture behavior of AlSi10Mg manufactured by selective laser melting: a review, Phys. Mesomech. 26 (2023) 367–390.
[7] S. Siddique, M. Awd, J. Tenkamp, F. Walther, High and very high cycle fatigue failure mechanisms in selective laser melted aluminum alloys, J. Mater. Res. 32 (2017) 4296–4304.
[8] M. Matušů, L. Džuberová, J. Papuga, J. Rosenthal, J. Šimota, L. Beránek, Fatigue analysis and heat treatment comparison of additively manufactured specimens from AlSi10Mg alloy, Int. J. Fatigue 185 (2024) 108357.
[9] S. Romano, A. Brückner-Foit, A. Brandão, J. Gumpinger, T. Ghidini, S. Beretta, Fatigue properties of AlSi10Mg obtained by additive manufacturing: defect-based modelling and prediction of fatigue strength, Eng. Fracture Mech. 187 (2018) 165–189.
[10] R.F. Fernandes, J.S. Jesus, L.P. Borrego, J.A. Ferreira, D. Neto, R. Branco, J. D. Costa, Notch sensitivity and heat treatment effect on the fatigue behaviour of AlSi10Mg aluminium alloy processed by additive manufacturing, Theor. Appl. Fract. Mec. 133 (2024) 104553.
[11] I. Roveda, I. Serrano-Munoz, J. Haubrich, G. Requena, M. Madia, Investigation on the fatigue strength of AlSi10Mg fabricated by PBF-LB/M and subjected to low temperature heat treatments, Mater. Des. 244 (2024) 113170.
[12] S. Baig, R. Ghiaasiaan, S. Shao, N. Shamsaei, Tensile and fatigue behaviors of additively manufactured AlSi10Mg: Effect of solutionizing and aging heat treatments, Fatigue & Fracture of Engineering Materials & Structures 46 (2023) 2662–2680.
[13] G. Nicoletto, Fatigue behavior of L-PBF metals: cost-effective characterization via specimen miniaturization, J. Mater. Eng. Perform. 30 (2021) 5227–5234.
[14] G. Nicoletto, Directional and notch effects on the fatigue behavior of as-built DMLS Ti6Al4V, Int. J. Fatigue 106 (2018) 124–131.
[15] G. Nicoletto, Influence of rough as-build surfaces on smooth and notched fatigue behavior of L-PBF AlSi10Mg, Addit. Manuf. 34 (2020) 101251.
[16] K. Shiozawa, L. Lu, Effect of non-metallic inclusion size and residual stresses on gigacycle fatigue properties in high strength steel, AMR 44–46 (2008) 33–42.
[17] Y. Murakami, Material defects as the basis of fatigue design, Int. J. Fatigue 41 (2012) 2–10.
[18] U. Zerbst, M. Vormwald, R. Pippan, H.-P. Gänser, C. Sarrazin-Baudoux, M. Madia, About the fatigue crack propagation threshold of metals as a design criterion – a review, Eng. Fract. Mech. 153 (2016) 190–243.
[19] H. Noguchi, K. Morishige, T. Fujii, T. Kawazoe, S. Hamada, Proposal of method for estimation stress intensity factor range on small crack for light metals, 15–20 July JSMS Annual Meeting (2007).
[20] Y. Murakami, Effect of hardness HV on fatigue limits of materials containing defects, and fatigue limit prediction equations, Metal Fatigue, Elsevier (2002) 57–74.
[21] A. Ueno, S. Miyakawa, K. Yamada, T. Sugiyama, Fatigue behavior of die casting aluminum alloys in air and vacuum, Procedia Eng. 2 (2010) 1937–1943.
[22] M. Fousová, D. Dvorský, A. Michalcová, D. Vojtěch, Changes in the microstructure and mechanical properties of additively manufactured AlSi10Mg alloy after exposure to elevated temperatures, Materials Characterization 137 (2018) 119–126.
[23] A. Nammalvar Raja Rajan, M. Krochmal, T. Wegener, A. Biswas, A. Hartmaier, T. Niendorf, G. Moeini, Micromechanical modeling of AlSi10Mg processed by laser-based additive manufacturing: From as-built to heat-treated microstructures, Materials 15 (2022).
[24] Z. Yang, A. Maurey, J. Kang, D.S. Wilkinson, 2D and 3D characterization of pore defects in die cast AM60, Materials Characterization 114 (2016) 254–262.
[25] H. Wu, J. Li, Z. Wei, P. Wei, Effect of processing parameters on forming defects during selective laser melting of AlSi10Mg powder, Rapid Prototyp. J. 26 (2020) 871–879.
[26] S. Romano, A. Abel, J. Gumpinger, A.D. Brandão, S. Beretta, Quality control of AlSi10Mg produced by SLM: Metallography versus CT scans for critical defect size assessment, Addit. Manuf. 28 (2019) 394–405.
[27] N.O. Larrosa, W. Wang, N. Read, M.H. Loretto, C. Evans, J. Carr, U. Tradowsky, M. M. Attallah, P.J. Withers, Linking microstructure and processing defects to mechanical properties of selectively laser melted AlSi10Mg alloy, Theor. Appl. Fract. Mech. 98 (2018) 123–133.
[28] J. Bao, Z. Wu, S. Wu, D. Hu, W. Sun, R. Wang, The role of defects on tensile deformation and fracture mechanisms of AM AlSi10Mg alloy at room temperature and 250 °C, Eng. Fract. Mech. 261 (2022) 108215.
[29] J. Tenkamp, S. Stammkötter, M. Merghany, F. Walther, Uniform fatigue damage tolerance assessment for additively manufactured and cast Al-Si alloys: size and mean stress effects, Addit. Manuf. Lett. 3 (2022) 100076.
[30] J. Tenkamp, F. Stern, F. Walther, Uniform fatigue damage tolerance assessment for additively manufactured and cast Al-Si alloys: an elastic-plastic fracture mechanical approach, Addit. Manuf. Lett. 3 (2022) 100054.
[31] M. Merghany, M. Teschke, F. Stern, J. Tenkamp, F. Walther, Assessing the lightweight potential of additively manufactured metals by density-specific Woehler and Shiozawa Diagrams, Front. Mech. Eng. 8 (2022).
[32] S. Siddique, M. Imran, F. Walther, Very high cycle fatigue and fatigue crack propagation behavior of selective laser melted AlSi12 alloy, Int. J. Fatigue 94 (2017) 246–254.
[33] F. Sausto, P.E. Carrion, N. Shamsaei, S. Beretta, Fatigue failure mechanisms for AlSi10Mg manufactured by L-PBF under axial and torsional loads: the role of defects and residual stresses, Int. J. Fatigue 162 (2022) 106903.

[34] K. Hussain, Short fatigue crack behaviour and analytical models: a review, Eng. Fract. Mech. 58 (1997) 327–354.
[35] H. Mayer, M. Papakyriacou, B. Zettl, S. Stanzl-Tschegg, Influence of porosity on the fatigue limit of die cast magnesium and aluminium alloys, Int. J. Fatigue 25 (2003) 245–256.
[36] S. Pearson, Initiation of fatigue cracks in commercial aluminium alloys and the subsequent propagation of very short cracks, Eng. Fract. Mech. 7 (1975) 235–247.
[37] K. Sadananda, M. Nani Babu, A.K. Vasudevan, A review of fatigue crack growth resistance in the short crack growth regime, Mater. Sci. Eng.: A 754 (2019) 674–701.
[38] J. Maierhofer, R. Pippan, H.-P. Gänser, Modified NASGRO equation for physically short cracks, Int. J. Fatigue 59 (2014) 200–207.
[39] A. Pourheidar, L. Patriarca, M. Madia, T. Werner, S. Beretta, Progress in the measurement of the cyclic R-curve and its application to fatigue assessment, Eng. Fract. Mech. 260 (2022) 108122.